Antarct. Meteorite Res., **10**, 249–274, 1997

IN SITU ANALYSIS OF OXYGEN ISOTOPES AND Fe/Mg RATIOS IN OLIVINE USING SIMS: PRELIMINARY RESULTS FOR AN ALLENDE CHONDRULE

Hajime HIYAGON

Department of Earth and Planetary Physics, The University of Tokyo, 11–16, Yayoi 2-chome, Bunkyo-ku, Tokyo 113

Abstract: A secondary ion mass spectrometer (SIMS; CAMECA ims-6f) was used for *in situ* spot analyses of chemical and oxygen isotopic compositions in olivine. San Carlos olivine and Burma spinel were used for oxygen isotope standards. Repeated analyses of oxygen isotopes were performed using these terrestrial standards by changing several factors which might control instrumental mass fractionation (such as entrance slit position, field aperture position, etc.) and conditions required for reproducible oxygen isotope analysis were investigated. For an optimum condition, the results of ~40 min analyses were reproducible within $\pm 3‰$ (1σ) for $^{17}O/^{16}O$ and $\pm 2‰$ (1σ) for $^{18}O/^{16}O$. For chemical composition (*e.g.*, Fe/Mg ratio) analyses, calibration was made using various terrestrial olivine grains with EPMA data. The oxygen isotope and Fe/Mg ratio analyses were performed for olivine grains in an Allende chondrule, which seems to be a compound chondrule consisting of two parts, (I) and (II). The results show that most of the analyzed points (14 out of 17 points) have relatively ^{16}O-rich compositions ($\delta^{17}O = -14$ to $-4‰$ and $\delta^{18}O = -10$ to $-5‰$), while three points near the edge of the chondrule (two points belong to (I) and one belongs to (II)) have relatively ^{16}O-poor compositions ($\delta^{17}O = -6$ to $-1‰$ and $\delta^{18}O = \sim 0‰$). The latter three points are more FeO-rich (the Fe/(Fe+Mg) atomic ratios of 4.5–8.2%) than the others (1.6–4.4%; mostly <3.2%). The present results, though rather preliminary, suggest that there is heterogeneity in oxygen isotopic composition even within a single chondrule.

1. Introduction

Since the work of CLAYTON *et al.* (1973, 1976), it has been revealed that meteorites and their constituents have variable oxygen isotopic compositions, suggesting the presence of several isotopically distinct reservoirs (see *e.g.*, CLAYTON, 1993). The conventional oxygen isotopic analyses using gas mass spectrometry requires a sample of at least ~mg size, and hence the data represent averages of the >mm sized areas. In this respect, recent development of secondary ion mass spectrometry (SIMS) provides a valuable tool for the analysis of much finer distribution of oxygen isotopic compositions. A number of SIMS studies have been done for oxygen isotopic compositions in various mineral separates, using a technique of pressing the grains in gold foil to avoid charging effect (*e.g.*, MCKEEGAN, 1987a; FAHEY *et al.*, 1987; ANDERS *et al.*, 1991; VIRAG *et al.*, 1991; WEINBRUCH *et al.*, 1993; HUTCHEON *et al.*, 1994; HUSS *et al.*, 1994; KURAT *et al.*, 1994; HOPPE *et al.*, 1995a, b). However, *in situ* analysis of oxygen isotopic compositions in meteorites using SIMS techniques appeared only

recently (HERVIG and STEELE, 1992, 1995; YURIMOTO *et al.*, 1994; SAXTON *et al.*, 1995, 1996; MCKEEGAN *et al.*, 1996; CHOI *et al.*, 1997; LESHIN *et al.*, 1997).

WEINBRUCH *et al.* (1993) separated olivine grains from different parts of the Allende chondrite and applied a SIMS analysis (with gold foil technique) to these grains. They found that refractory forsterites and forsteritic cores of isolated olivine grains have relatively ^{16}O-rich compositions (δ^{17}O down to $-12‰$ and δ^{18}O down to $-9‰$) but that fayalite-rich rims of isolated olivine grains and most of the matrix olivines have less ^{16}O-rich compositions (δ^{17}O $\sim-3‰$ and δ^{18}O $\sim0‰$). Their results for refractory forsterite show much higher ^{16}O-enrichment than the results for chondrules obtained by RUBIN *et al.* (1990) using conventional mass spectrometry (δ^{18}O down to $\sim-3‰$). Recently, *in situ* analysis of oxygen isotopes in isolated olivine grains from Allende, Ornans and Murchison was conducted by HERVIG and STEELE (1992, 1995). They analyzed olivine grains in thin sections using an electron gun for charge compensation and applying a high energy offset of >300 V to minimize the effect of molecular (OH) ions, and obtained results similar to those of WEINBRUCH *et al.* (1993). SAXTON *et al.* (1995, 1996) also analyzed olivine grains in Allende and Julesburg using SIMS (the Manchester ISOLAB 54 ion probe) with a multi-ion-collection system. They also observed a similar ^{16}O-enrichment for forsteritic olivine grains in Allende, but found that isolated olivine grains from Julesburg have more variable oxygen isotopic signatures among the grains.

For CAIs, *in situ* analyses of oxygen isotopes were conducted by YURIMOTO *et al.* (1994) using a CAMECA ims-3f with a negative Au ion primary beam (only for ^{18}O/^{16}O ratios) and by MCKEEGAN *et al.* (1996) using a CAMECA ims-1270 with a Cs^+ primary beam and an electron gun. MCKEEGAN *et al.* (1996) used a Faraday cup for detecting ^{16}O ions and an electron-multiplier-based ion counting system for detecting ^{17}O and ^{18}O ions, and succeeded in analyzing oxygen isotopic ratios with a precision at $\sim1‰$ level. (See also CHOI *et al.* (1997) and LESHIN *et al.* (1997).)

The technique of *in situ* analysis of oxygen isotopic compositions using SIMS is rather new and several laboratories are trying to develop the technique. Although the precision of this technique is still one order of magnitude worse than that of conventional mass spectrometry, the capability of analyzing small areas in thin sections has great advantage in the study of meteorites and the early solar system. Considering this importance, I also decided to develop the technique of *in situ* analysis of oxygen isotopes using CAMECA ims-6f, a newly installed ion microprobe in the University of Tokyo. This is the first report of the results obtained with this instrument, and hence details of the analytical techniques are described.

2. Experimental

2.1. Analytical techniques

A secondary ion mass spectrometer (SIMS), CAMECA ims-6f in the University of Tokyo installed in March 1995, was used in the present study. All the samples were prepared as thin sections, whose surfaces were polished and gold coated (~600 Å thick). A Cs^+ primary beam of +10 kV energy was used both for oxygen isotope and chemical composition analyses. A defocused beam, limited by an aperture to form a

circular shaped beam with relatively homogeneous intensity, was used for the analysis. The beam size was 50–80 μm in diameter and the beam intensity was 0.9–1.9 nA for oxygen isotope analyses and 0.5–1 nA for chemical composition analyses.

The beam position was checked using an optical lens with a CCD camera, with which the sputtered area (*i.e.*, the beam position) was clearly identified on the gold-coated sample surface. The oxygen isotope analysis and the chemical composition analysis for an Allende chondrule were conducted at different times, but the analyzed positions were exactly the same. This was possible by looking at the secondary ion image of $^{16}O^-$. Gold coating was sputtered away from the area once analyzed, so that the area gave a bright circular image of secondary $^{16}O^-$ ions, and hence it was not difficult to position the new beam exactly on the same position once analyzed.

Negative secondary ions were accelerated at -9.5 kV. They were limited by a "field aperture" which was placed in the sample image plane in the secondary ion optics so that the analyzed area was restricted to the center area of the primary beam. The size of the analyzed area was ~12 $\mu m\phi$ for oxygen isotope analysis and ~33 $\mu m\phi$ for the chemical composition analysis. Analyzing only the center area of the beam is important to minimize the effect of $^{16}O^1H$ peak at mass 17, because hydrogen mostly exists as surface contamination and comes from the edge of the beam. This also reduces dispersion of the angle of secondary ion beam trajectories resulting in reducing the aberration, and hence, is helpful to obtain the high mass resolution required for oxygen isotope analysis. The mass resolving power (MRP) was set to be ~5500 at 10% level of the peak for the oxygen isotope analysis to separate ^{17}O and $^{16}O^1H$ peaks and ~3000 for the chemical composition analysis.

The secondary ion beam was then energy-filtered with an electrostatic analyzer (ESA) and an energy slit placed after ESA. The energy slit was first centered on the position of the maximum beam intensity and then opened wide to have an energy window of ~100 V. Using a large energy window is important to minimize the effect of energy-dependent instrumental mass fractionation, which is reported by many authors (*e.g.*, SHIMIZU and HART, 1982; JULL, 1982; GNAZER and HUTCHEON, 1988a). A similar effect was also observed in a preliminary experiment of the present work, where Ti isotopes in Ti metal standard were analyzed as positive ions at 10 kV, using a narrow energy window of ~4 V, and applying variable energy offset. The results show that the mass fractionation factor is highly dependent on energies of secondary ions; the observed mass fractionation factors are about -20‰/amu for zero-offset ions, about -10‰/amu for high energy ions ($+30$ V) and about -30‰/amu for low energy ions (-5 V) (HIYAGON, 1996).

The combination of a positive primary beam and a negative sample voltage for accelerating negative secondary ions would produce severe charge-up on the surface of an insulating sample. A normal-incidence electron gun (NEG) was used to compensate the charge-up effect. Electrons were accelerated at an energy of -9.5 kV, exactly the same as the secondary ion acceleration voltage, and an electron cloud of zero energy was formed just above the sample surface, which would automatically compensate the charge-up on the sample surface. The size of the electron beam was 125–150 $\mu m\phi$ During operation of NEG, three coils (Bya, Byb and Bya') on the secondary ion optics and an additional coil (Bx) placed beneath the sample chamber were

active. One coil (Bya) was used for changing the trajectory of the electron beam normal to the sample surface, but it also affected the trajectory of the secondary ions. Two coils (Byb and Bya') were used to correct the secondary ion trajectory back to the original path. Combination of these three coils enabled us to move the electron beam in y- (*i.e.*, vertical) direction on the sample surface without changing the secondary ion trajectory as a whole. Another small coil (Bx) was used for fine adjustment of the electron beam in x- (*i.e.*, horizontal) direction on the sample surface. (Note that the sample surface was placed vertically in the sample chamber and that the x- and y-directions on the sample surface correspond to horizontal and vertical directions, respectively.) Tuning of these coils was done very carefully, because using coils, or using magnetic fields, could cause additional mass fractionation. A good test to examine the tuning condition is to check the images of different ions having different masses (*e.g.*, H^- and O^- ions). If the coils are tuned correctly, the position of the secondary ion image does not move when switching from one mass to another. Although such a perfect tuning is difficult to attain, I made best effort to minimize the movement of the sample image before the analysis.

The secondary ions were finally mass-separated and detected with an electron multiplier (EM) operated in a pulse counting mode. In the oxygen isotope analysis, the peaks of three oxygen isotopes and $^{16}O^1H$ were analyzed. The intensity of the $^{16}O^1H$ peak was much higher than that of the ^{17}O peak at the beginning of each analysis, but decreased to the level of the ^{17}O peak after 10–15 min of sputtering the sample surface, and by that time the intensities of the O^- secondary beams became stable enough for the isotope analysis. Contribution of the tail of the $^{16}O^1H$ peak at the center position of the ^{17}O peak was negligibly small (<0.1‰) and thus no correction was made for this interference. Typical high resolution mass spectra of oxygen isotope peaks are shown in Fig. 1. Note that each peak has a good flat top and that ^{17}O and $^{16}O^1H$ peaks are clearly separated from each other.

After determining the center of each peak, the intensity was analyzed in the order ^{16}O, ^{17}O, $^{16}O^1H$ and ^{18}O repeatedly by peak jumping for a total of 200 cycles, consisting of 10 blocks with 20 cycles each. The magnet control was very stable so that

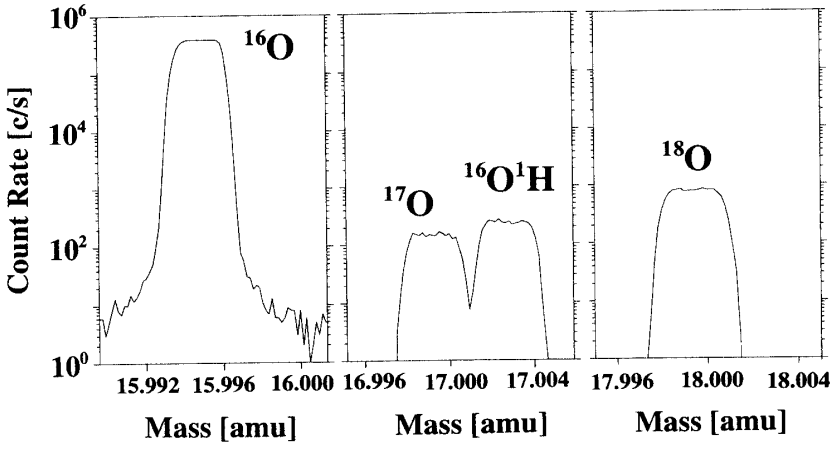

Fig. 1. Typical mass spectra of oxygen isotope peaks at MRP~5000.

the peak centering was done only once at the beginning of each analysis. In fact, the field value for each peak was stable for one hour within ±1 digit (*i.e.*, corresponding to ΔM ~0.0002 amu for the region of mass 16), which was small compared with the length of the flat top (~10 digits). In each cycle, the waiting times for stabilizing the magnetic field for ^{16}O, ^{17}O, $^{16}O^1H$ and ^{18}O peaks were 0.8 s, 0.5 s, 0.1 s and 0.5 s, respectively, and the integration times for ion counting were 1 s, 3 s, 0.5 s and 2 s, respectively. The intensity of the ^{16}O peak, and also those of the ^{17}O and ^{18}O peaks, was very stable within a few % during the whole analysis (typically ~40 min), which corresponds to an intensity change of only ~0.1‰ or less for each cycle. Hence, the intensity change of the normalization isotope (^{16}O) within one cycle was ignored and the ratios of $^{17}O/^{16}O$ and $^{18}O/^{16}O$ were calculated simply by taking the ratios of the observed intensities in each cycle. The final results of the $^{17}O/^{16}O$ and $^{18}O/^{16}O$ ratios were obtained by averaging the ratios for all the cycles, but some data with $>3\sigma$ deviations from the average were rejected, where σ denotes the standard deviation. The uncertainty of the average thus calculated is given by $\sigma/(n-1)^{1/2}$, where n is the total number of the accepted data.

The analytical condition for the chemical composition analysis was very similar to that for the oxygen isotope analysis, except that the former was performed with a mass resolving power (MRP) of ~3000. An O^- primary beam is often used for the analysis of an insulating sample. However, in order to preserve the oxygen isotope signature of the sample, the present analysis was performed with a Cs^+ primary beam and an electron gun. In this condition, however, some elements (*e.g.*, Mg) have very low efficiencies of forming negative ions, and hence, oxide ions (*e.g.*, MgO^-) instead of atomic ions (*e.g.*, Mg^-) were analyzed. The analyzed ions were ^{27}Al, ^{28}Si, $^{26}Mg^{16}O$, $^{28}Si^{16}O$, ^{56}Fe, $^{24}Mg^{16}O_2$, ^{60}Ni, $^{28}Si^{16}O_2$, $^{56}Fe^{16}O$, $^{60}Ni^{16}O$, $^{28}Si^{16}O_3$, $^{44}Ca_2$ (+ ^{88}Sr) and $^{56}Fe^{16}O_2$. Typical mass spectra of the analyzed elements and molecules with some interfering peaks are shown in Fig. 2 (mass spectra for San Carlos olivine). Each analysis consisted of a total of 25 cycles (5 cycles × 5 blocks) and took about 10 min. The ^{27}Al peak decreased with time and is considered to be mostly instrumental contamination. The chemical composition analyses were applied to some terrestrial olivine standards of known compositions (measured with EPMA, see Table 1) and the observed intensity ratios of $^{56}Fe^{16}O/^{26}Mg^{16}O$, $^{56}Fe^{16}O_2/^{24}Mg^{16}O_2$, etc., by SIMS were compared with the Fe/Mg atomic ratios calculated from the EPMA data. Also the ratios of $^{60}Ni^{16}O/^{28}Si^{16}O$, etc., measured with SIMS were compared with the Ni/Si atomic ratios by EPMA.

All the data were corrected for the dead time (τ) of the ion counting system. The probability of incoming ions can be treated as that for a randomly occurring process, which obeys the Poisson distribution (*e.g.*, McKEEGAN *et al.*, 1985), and the measured count rate (C_m) is related to the true count rate (C_t) in the form: $C_m = C_t \exp(-\tau C_t)$. Here τC_m is less than a few $\times 10^{-2}$ for a typical dead time of 20–30 ns and a count rate of ≤ several $\times 10^5$ cps. Hence, the true count rate can be obtained in good approximation by

$$C_t \approx C_m \exp(\tau C_m \exp(\tau C_m \exp(\tau C_m \exp(\tau C_m)))), \quad (1)$$

(see *e.g.*, McKEEGAN, 1987b).

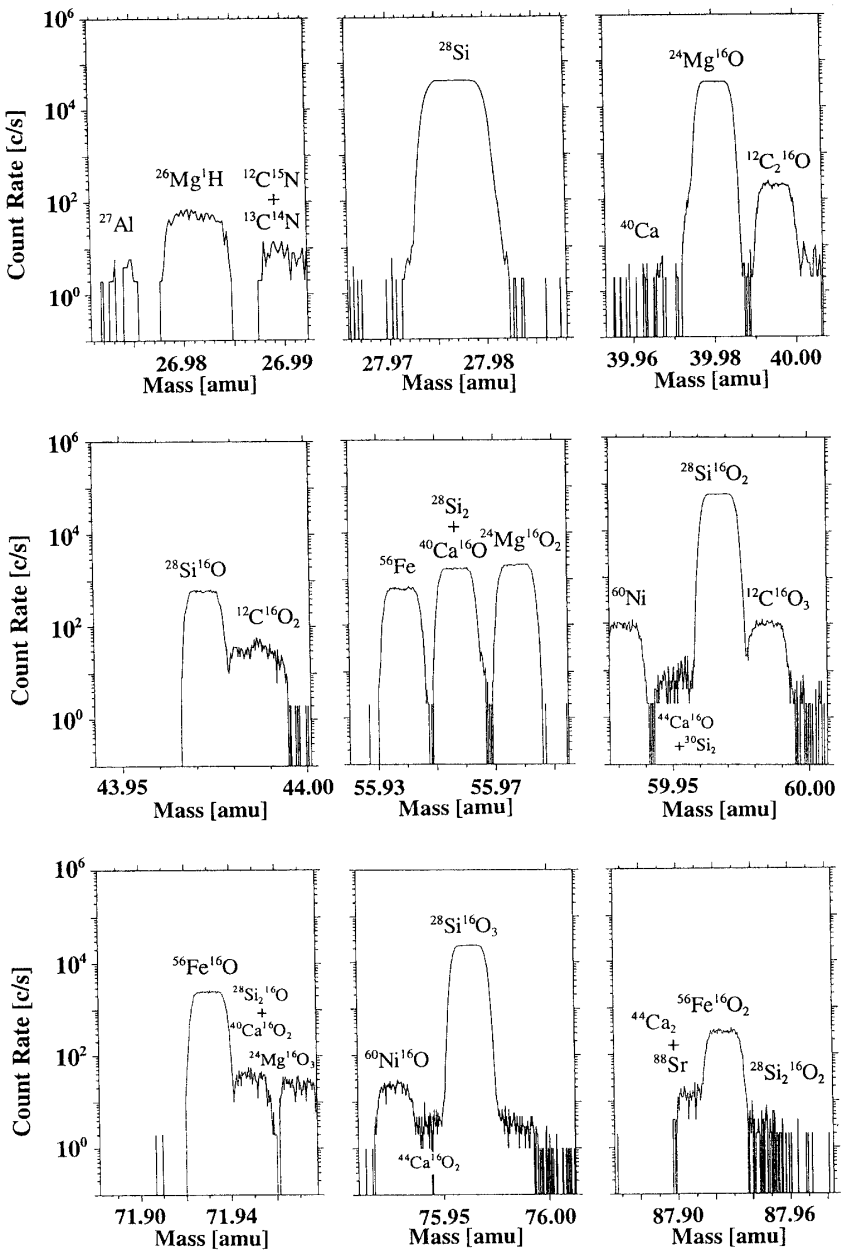

Fig. 2. Mass spectra of negative ion peaks from San Carlos olivine obtained at MRP~3000.

It may also be useful to expand this equation in τC_m. Then we obtain:

$$C_t \approx C_m\{1 + \tau C_m + (3/2)(\tau C_m)^2 + (8/3)(\tau C_m)^3\}. \quad (2)$$

The dead time was determined by Ti isotope measurements using Ti metal standard (see below for details of this procedure). The analysis was performed with an O^- primary beam of -12.5 kV energy and measuring positive ions of Ti-isotopes accelerated at $+10$ kV. A mass resolving power of ~5000 was applied to separate Ti and Ti-hydride peaks.

The estimated dead time was ~25 ns in November 1995 (HIYAGON, 1996), but it

Table 1. Chemical compositions of terrestrial olivine standards.*

Samples**	Synthetic forsterite	Iwanai dunite	San Carlos olivine	Miyake olivine	Ol#14	Ol#15
No. of analysis:	9	9	9	9	9	9
SiO_2	41.350 ±0.109	40.423 ±0.292	39.996 ±0.140	39.375 ±0.103	38.793 ±0.176	38.294 ±0.296
TiO_2	(0.01)	(0.00)	(0.00)	(0.01)	(0.00)	(0.01)
Al_2O_3	(0.00)	(0.00)	(0.02)	(0.01)	(0.00)	(0.00)
FeO	0.009 ±0.002	5.962 ±0.254	8.918 ±0.036	13.999 ±0.167	17.305 ±0.510	20.426 ±0.363
MnO	0.000 ±0.000	0.093 ±0.005	0.128 ±0.001	0.229 ±0.002	0.268 ±0.010	0.306 ±0.007
MgO	58.025 ±0.131	53.148 ±0.342	50.844 ±0.275	46.652 ±0.117	44.055 ±0.481	41.528 ±0.387
CaO	0.005 ±0.002	0.016 ±0.012	0.067 ±0.001	0.223 ±0.003	0.036 ±0.003	0.044 ±0.012
Na_2O	(0.00)	(0.00)	(0.00)	(0.00)	(0.01)	(0.00)
K_2O	(0.01)	(0.01)	(0.00)	(0.01)	(0.01)	(0.01)
Cr_2O_3	(0.01)	(0.02)	(0.04)	(0.02)	(0.00)	(0.00)
NiO	0.001 ±0.001	0.412 ±0.009	0.370 ±0.003	0.086 ±0.001	0.139 ±0.002	0.099 ±0.004
Total	99.390 ±0.209	100.054 ±0.218	100.324 ±0.412	100.565 ±0.346	100.596 ±0.365	100.698 ±0.501

*Weight % compositions analyzed with EPMA. Data in the parentheses were obtained with an electron energy of 15 kV (single analysis). Data with errors (1σ) are averages of 9 analyses conducted with a 25 kV electron beam.

**Samples are: synthetic forsterite, Iwanai dunite, San Carlos olivine, Miyake olivine and two olivine grains separated from gabbro.

became 38–40 ns in the period of April–June of 1996, when the lifetime of the first electron multiplier (EM) was approaching its end. In fact, a high voltage of ~3 kV must be applied to the EM in this period. In this condition, it was observed that the oxygen isotope measurements became less reproducible after an analysis was performed with a high count rate (*e.g.*, ^{16}O ~9×10^5 cps). The cause for this is probably the changes in the EM condition and hence in the dead time. The first EM was finally replaced by a new one when an accidental vacuum loss occurred on June 21, 1996. All the oxygen isotope analyses shown below were performed with the new EM, but all the chemical composition analyses were performed with the first EM. The dead time of the ion counting system using the new EM was, as will be described below, 28.1 ± 0.2 ns and independent of the count rate. The EM was operated at ~2.1 kV and seemed fairly stable. However, to minimize a possible change in the EM condition as described above, only moderate count rates of $(4–5)\times10^5$ cps were applied for the oxygen isotope measurements.

2.2. *Dead time determination using Ti isotopes*

The measured Ti isotopic ratios were compared with the true (literature) ratios given by NIEDERER *et al.* (1981), that is, $^{46}Ti/^{48}Ti=0.108548$, $^{47}Ti/^{48}Ti=0.099315$, $^{49}Ti/^{48}Ti=0.074463$ and $^{50}Ti/^{48}Ti=0.072418$. Apparently the measured ratios deviated

from the true values because of (1) the instrumental mass fractionation and (2) the dead time. The dead time correction is most significant for ^{48}Ti due to its high abundance and is less important for the other four isotopes. Ignoring the latter, the measured four ratios require identical dead time corrections on ^{48}Ti. For Ti isotopes, it is reported that the instrumental mass fractionation obeys an "exponential" law rather than a linear law (FAHEY *et al.*, 1987). The "exponential" law is expressed by the formula:

$$(^{k}\mathrm{Ti}/^{48}\mathrm{Ti})_{\mathrm{instr}}/(^{k}\mathrm{Ti}/^{48}\mathrm{Ti})_{o}=(k/48)^{\alpha},\ (k=46,\ 47,\ 49 \text{ and } 50), \tag{3}$$

where subscript "instr" refers to the instrumentally fractionated ratio (*i.e.*, the dead time-corrected measured ratio) and subscript "o" refers to the true ratio. Using the measured ratios of $(^{k}\mathrm{Ti}/^{48}\mathrm{Ti})_{m}$ without any dead time correction, a plot of $\ln\{(^{k}\mathrm{Ti}/^{48}\mathrm{Ti})_{\mathrm{instr}}/(^{k}\mathrm{Ti}/^{48}\mathrm{Ti})_{o}\}$ *vs* α ln(k/48) gives a linear trend, but the line does not pass through the origin. It is because the counting loss of ^{48}Ti increases all the measured ratios of $(^{k}\mathrm{Ti}/^{48}\mathrm{Ti})_{m}$ with a similar amount. By applying the least squares fitting, the amount of dead time correction on ^{48}Ti can be estimated from the y-intercept of the fitted line, so that the dead time τ can be calculated for a given ^{48}Ti count rate. In order to obtain accurate dead time, a dead time correction is made to other Ti isotopes as well, and then the least squares fitting is applied again. Several iterations of such procedures would improve the estimate of τ.

As is shown in Fig. 3, the dead time obtained is independent of the count rate of ^{48}Ti with the average of 28.1$\pm$0.2 ns (2σ error). It is not certain, however, whether the dead time obtained for Ti^{+} ions at 10 kV can be directly applicable to the dead time for O^{-} ions at -9.5 kV. In fact, it is reported that the dead time may depend on elements, polarities and types of ions (atomic or molecular), and so on (ZINNER *et al.*, 1986). Although it may also be possible to determine the dead time using O^{-} ions, the result would have a larger uncertainty. In this study, therefore, the dead time

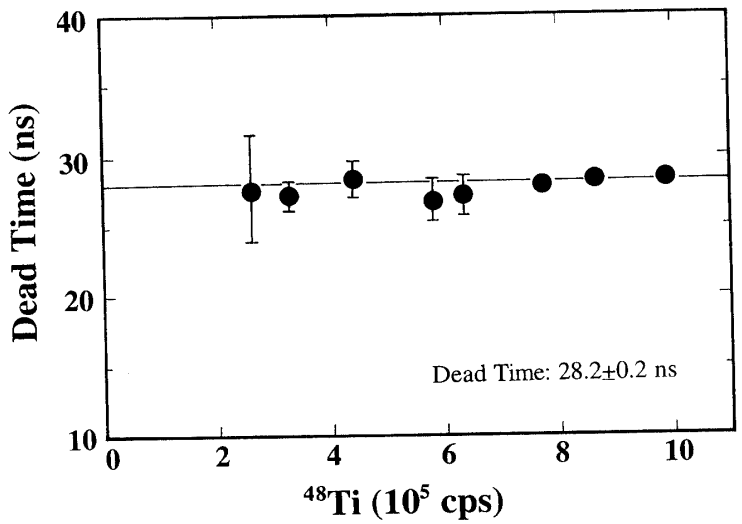

Fig. 3. The dead time of the ion counting system determined using Ti isotope analyses for Ti metal standard. Note that the dead time is almost independent of the count rate of ^{48}Ti.

obtained for Ti^+ ions was adopted for oxygen isotope analysis. As will be shown later, the $\delta^{17}O$ and $\delta^{18}O$ ratios thus obtained for San Carlos olivine are well explained by a mass fractionation from its true ratios, suggesting that the dead time correction adopted here worked well for oxygen isotopes.

However, in order to minimize the effect of the dead time correction, all oxygen isotope analyses both for the terrestrial standards and samples were performed at similar count rates of $^{16}O^-$ ions, *i.e.*, typically $(4–5)\times10^5$ cps. This greatly reduces the effect of the uncertainty in the estimated dead time, because dead time corrections are canceled out when the results for the samples are normalized to those for the terrestrial standards.

2.3. Reproducibility tests for oxygen isotope analysis

In the course of repeated analyses of oxygen isotopes using terrestrial standards (San Carlos olivine and Burma spinel), it was found that the field aperture position is important for obtaining reproducible results. When the analyzed area was off-centered in the primary beam spot, the results often showed a large instrumental mass fractionation. An example is demonstrated in *Appendix A*, where the observed $^{18}O/^{16}O$ ratios show variations of up to ~10‰ depending on the field aperture position. In extreme cases when the edge of the beam was observed, variations of the measured ratios were as much as ~15‰ for $^{17}O/^{16}O$ and ~30‰ for $^{18}O/^{16}O$. In such cases, the crossover image (*i.e.*, the distribution of the beam intensity at the entrance slit position, where the secondary ion beam converges) generally was not symmetric (Gaussian) but heterogeneous. The crossover image is related to the distribution of the horizontal (=parallel to the sample surface) component of the initial energy of secondary ions (SLODZIAN, 1980). Since the initial energy of ions and their emission angle may have mass dependence, heterogeneity in the crossover image may produce additional mass fractionation effect.

It was also found that the entrance slit position is another important factor controlling the instrumental mass fractionation, especially when the slit width is set narrow to obtain a high mass resolution. An example is demonstrated in *Appendix B*. This may also be understood in terms of mass dependence in the initial energy and emission angle of the secondary ions. When the entrance slit width is set narrow, only a small part of the beam at the crossover position is analyzed. In such a case, the analyzed area of the beam may not be representative of the beam as a whole, and this may affect instrumental mass fractionation. Therefore, it is crucial for a reproducible analysis at high mass resolution that the entrance slit is always positioned at the center of the symmetrical crossover image. In the present oxygen isotope analysis, centering of the entrance slit position was done each time at the beginning of the analysis by monitoring the intensity of the $^{16}O^-$ beam.

Heterogeneity in the primary beam may also affect the crossover image and hence the instrumental mass fractionation for a similar reason. Furthermore, it would also change flatness of the sample surface, resulting in possible changes in the mass fractionation factor with time. Hence, in the present study, the primary beam was tuned carefully to get good homogeneity.

As was already mentioned, the coils of the normal-incidence electron gun could

cause additional mass fractionation. Furthermore, it was also observed that the electron beam also affected the secondary ion image. Therefore, homogeneity of the electron beam may also be an important factor for reproducible analyses, though reproducibility tests have not been conducted by changing the shape of the electron beam. (During the reproducibility tests of oxygen isotope analysis, it was observed that the position of the electron beam in fact affected the intensity of the $^{16}O^-$ beam by up to ~3.5%. Unfortunately, it was not checked if it also affected the instrumental mass fractionation at the same time.) In the present study, therefore, the electron beam was tuned to be as homogeneous as possible and was centered on the primary beam position.

Recently, an experiment was conducted to examine the mass fractionation effect on oxygen isotopes at the initial stage of sputtering, when the intensity of the $^{16}O^-$ ions was still increasing towards its steady-state value. The results show unexpectedly high mass fractionation for the first 10–15 min (see *Appendix C*). Note, however, that the oxygen isotope analyses in the present study were performed after the $^{16}O^-$ beam intensity became very stable. (It generally took >15 min before starting the analysis.) Hence, this effect may not be important in the present analysis for the Allende chondrule. In fact, reproducibility of the oxygen isotope data for San Carlos olivine analyzed with the same condition as that for the Allende chondrule is fairly good (see Table 2), suggesting this effect, if present, was not significant in the present study.

After careful adjustment of the primary beam, secondary ion optics, the electron gun, etc., the measured oxygen isotopic ratios became reproducible within ~3‰ for $^{17}O/^{16}O$ and ~2‰ for $^{18}O/^{16}O$ for an analysis of ~40 min (values are 1σ). These values are approaching the uncertainties due to counting statistics (see Table 2).

In order to minimize the effect of the instrumental mass fractionation stated above, it is desirable to analyze a sample and a standard at the same time with the same primary beam and with the same condition in the secondary ion optics. In the present study, oxygen isotope analyses were performed both for an Allende chondrule and for San Carlos olivine standard in three successive days (from June 28 to 30, 1996) without changing the conditions of the instrument. The size and intensity of the primary beam was ~80 μm in diameter and 1.0–1.3 nA, respectively, throughout this period. San Carlos olivine standard was analyzed repeatedly before and after the Allende chondrule analysis to check the stability of the instrumental mass fractionation. The results were reproducible within ~3‰ for $^{17}O/^{16}O$ and ~2‰ for $^{18}O/^{16}O$ (1σ) (Table 2).

Using the obtained $\delta^{17}O$ and $\delta^{18}O$ values for San Carlos olivine (Table 2) and comparing them with the true values, a test can be conducted to see whether the dead time correction (based on Ti isotope data) is well applied to oxygen isotopes. If the dead time correction is appropriate, the two sets of data should be combined with each other by a mass fractionation law. The absolute value of the terrestrial $^{17}O/^{16}O$ ratio is only poorly known. However, MCKEEGAN (1987b) estimated the $(^{17}O/^{16}O)_{SMOW}$ value to be $(3.8309 \pm 0.0034) \times 10^{-4}$ based on the repeated SIMS analyses on various terrestrial spinel and hibonite standards. SIMS data are generally mass-fractionated, but assuming a $(^{18}O/^{16}O)_{SMOW}$ value of 2.0052×10^{-3} (BAERTSCHI, 1976) and applying an exponential mass fractionation law to each data set, he obtained a precise estimate of the $(^{17}O/^{16}O)_{SMOW}$ value given above, which is probably the most precise figure at pre-

Table 2. Repeated analysis of San Carlos olivine standard.

Date (1996)	Position	Measured oxygen isotopic ratios $^{17}O/^{16}O$ (10^{-4})	$^{18}O/^{16}O$ (10^{-3})	$\delta^{17}O^{(4)}$ (‰)	$\delta^{18}O^{(4)}$ (‰)
June 28	(1) Pos.#1	3.8163±0.0089	1.9958±0.0030	3.2±2.3	5.2±1.5
	(1) Pos.#2	3.8119±0.0104	1.9936±0.0030	2.1±2.7	4.1±1.5
	(1) Pos.#2	3.8173±0.0080	1.9966±0.0027	3.5±2.1	5.6±1.3
	(1) Pos.#2	3.8096±0.0108	2.0011±0.0034	1.5±2.8	7.8±1.7
	(1) Pos.#2	3.8076±0.0081	1.9897±0.0029	1.0±2.1	2.1±1.4
	(1) Pos.#2	3.8116±0.0135	1.9929±0.0037	2.0±3.5	3.7±1.9
	(1) Pos.#2	3.8204±0.0105	1.9955±0.0031	4.3±2.7	5.0±1.5
June 29	(1) Pos.#3	3.8167±0.0099	1.9955±0.0030	3.3±2.6	5.1±1.5
	(1) Pos.#3	3.8183±0.0089	1.9939±0.0031	3.8±2.3	4.2±1.5
June 30	(2) Pos.#4	3.7947±0.0092	1.9934±0.0032	−2.4±2.4	4.0±1.6
	(2) Pos.#4	3.8253±0.0087	1.9978±0.0029	5.6±2.3	6.2±1.4
	(2) Pos.#4	3.8060±0.0109	1.9909±0.0038	0.5±2.8	2.7±1.9
	Average	3.8133±0.0080[3]	1.9948±0.0031[3]	2.44	4.70

(1) Analyzed before Allende chondrule analysis.
(2) Analyzed after Allende chondrule analysis.
(3) Used for normalization assuming $\delta^{17}O$=2.44‰ and $\delta^{18}O$=4.70‰ on the SMOW scale.
(4) δ-values (SMOW-scale) normalized to the average ratio.

sent. The oxygen isotopic compositions of San Carlos olivine and Burma spinel used in the present study were recently measured with gas mass spectrometry using a laser-fluorination technique, which gave $\delta^{17}O=+2.440\pm0.071$‰ and $\delta^{18}O=+4.700\pm0.081$‰ for the former and $\delta^{17}O=+12.210\pm0.026$‰ and $\delta^{18}O=+23.830\pm0.069$‰ for the latter on a SMOW scale (JABEEN and KUSAKABE, personal communication 1996). The $\delta^{18}O$ value for San Carlos olivine is similar to the value ($+4.88\pm0.06$‰ for 20 analyses) obtained by MATTEY and MACPHERSON (1993), but somewhat lower than the value ($+5.26\pm0.05$‰ for 2 analyses) obtained by EILER *et al.* (1995). The $\delta^{17}O$ and $\delta^{18}O$ values for Burma spinel are higher than the values ($\delta^{17}O=+11.6\pm0.2$‰ and $\delta^{18}O=+22.3\pm0.2$‰) obtained by R. N. CLAYTON and quoted in MCKEEGAN (1987) and in WEINBRUCH *et al.* (1993). It is not certain if these variations are due to variations in the samples or due to some problems in normalization to SMOW values. In the present study I adopted the values by JABEEN and KUSAKABE, because the samples they analyzed were the same grain of San Carlos olivine and several grains of Burma spinel from the same batch of the samples used in the present SIMS analysis. For Burma spinel, however, the grains they analyzed were not exactly the same as those used in the present study, so that some heterogeneity among different grains cannot be ruled out completely.

Using these values, $^{17}O/^{16}O$ and $^{18}O/^{16}O$ ratios for San Carlos olivine measured in the present study (Table 2) are examined. By comparing the observed $^{18}O/^{16}O$ ratio for San Carlos olivine ($(1.9948\pm0.0031)\times10^{-3}$) and its true value ($(2.0146\pm0.0002)\times10^{-3}$; $\delta^{18}O=4.70\pm0.08$‰), a mass fractionation factor for the SIMS analysis (assum-

ing an exponential mass fractionation law) can be calculated. Then, a $^{17}O/^{16}O$ ratio for San Carlos olivine expected for the SIMS analysis can be calculated from its true value ($(3.8402\pm0.0034)\times10^{-4}$; $\delta^{17}O=2.44\pm0.07‰$) to be $(3.8207\pm0.0034)\times10^{-4}$. This is consistent with the observed ratio ($(3.8133\pm0.0080)\times10^{-4}$) within the experimental uncertainty. This suggests that the dead time correction based on Ti isotope data also worked well for oxygen isotope data.

Repeated oxygen isotope analyses were performed for two standards, San Carlos olivine and Burma spinel, without changing the analytical conditions. If all the data are normalized to the averages of San Carlos olivine data ($\delta^{17}O=2.44‰$ and $\delta^{18}O=4.70‰$), the averages of the Burma spinel data are calculated to be $\delta^{17}O=9.3\pm3.2‰$ and $\delta^{18}O=22.2\pm3.8‰$ (errors are 2σ), which are consistent with the values by JABEEN and KUSKABE ($\delta^{17}O=12.21‰$ and $\delta^{18}O=23.83‰$) within experimental uncertainties. This is compatible with the reports that no matrix effect was detected between spinel and hibonite (MCKEEGAN, 1987b) or spinel and olivine (WEINBRUCH *et al.*, 1993).

2.4. *Calibration of Fe/Mg and Ni/Si ratios in olivine*

One synthetic forsterite and five terrestrial olivines with various chemical compositions, from Fo_{78} to Fo_{100}, were used for calibrating the chemical composition analysis with SIMS. The EPMA data for these olivine standards are shown in Table 1. All the EPMA analyses were first performed with an electron energy of 15 kV, resulting in relatively large uncertainties in Ni and other minor elements data. More precise EPMA analyses using a 25 kV electron beam were performed after the SIMS analyses on terrestrial olivine standards. For each olivine grain, Si, Fe, Mg, Ca, Ni and Mn were analyzed repeatedly (total of 9 analyses) for positions mostly near the spots already analyzed with SIMS. This greatly improved the quality of the EPMA data. Therefore, the new EPMA data obtained with a 25 kV electron beam are used in the present study, which are listed in Table 1 with 1σ errors. (The data for the other elements obtained with a 15 kV electron beam are listed in the parentheses.) The results of the SIMS analysis are summarized in Table 3. Three to five analyses were performed for each sample except for the synthetic forsterite. Errors are given as 1σ for the repeated analyses. Although no errors are shown for the synthetic forsterite data, they must be considered to have similar uncertainties. In Table 4, the results of the SIMS analysis (FeO/MgO, $^{58}Ni/Si$, etc.) are compared with the EPMA data (Fe/Mg and Ni/Si atomic ratios).

Atomic ratios of Fe/Mg and Ni/Si are related to the measured intensity ratios of corresponding metal or oxide ions in the SIMS analysis, such as $(Fe/Mg)_{atomic}=K_1\times(FeO/MgO)_{SIMS}$ and $(Ni/Si)_{atomic}=K_4\times(^{58}Ni/Si)_{SIMS}$, where K_1 and K_4 are considered to be "sensitivity factors". The "sensitivity factors" (K_1 to K_6) calculated for different combinations of peaks are summarized in Table 5. All the "sensitivity factors" are more or less constant for all the olivine standards with different chemical compositions. Good correlations between the EPMA data and the SIMS data can be seen in Fig. 4a, where the observed intensity ratios of $(FeO/MgO)_{SIMS}$ and $(Fe_2O/Mg_2O)_{SIMS}$ are plotted against $(Fe/Mg)_{atomic}$, and in Fig. 4b, where $(^{60}NiO/SiO)_{SIMS}$ is plotted against $(Ni/Si)_{atomic}$. Taking the averages of the "sensitivity factors" listed in Table 5, we obtain the following equations:

Table 3. Intensity ratios of selected peaks measured with SIMS for terrestrial olivines.*

Sample name	# of data	Fo number**	SiO/Si[10^{-2}]	SiO_2/Si	MgO_2/MgO[10^{-2}]	FeO/Fe	FeO_2/Fe	$^{58}Ni/^{60}NiO$
Synthetic forsterite	1	99.99	1.43	1.29	5.20	–	–	–
Iwanai dunite	4	93.70	1.40 ±0.04	1.35 ±0.10	5.71 ±0.13	3.98 ±0.07	32.3 ±1.4	12.1 ±0.2
San Carlos olivine	4	90.16	1.41 ±0.02	1.40 ±0.03	5.85 ±0.06	3.98 ±0.06	31.7 ±0.9	12.5 ±0.8
Miyake olivine	3	83.16	1.34 ±0.00	1.38 ±0.07	5.97 ±0.11	3.92 ±0.05	30.0 ±1.0	12.3 ±0.3
Ol#14	5	77.95	1.30 ±0.01	1.39 ±0.08	6.05 ±0.15	3.97 ±0.00	29.0 ±0.7	12.6 ±0.2
Ol#15	3	72.39	1.32 ±0.01	1.55 ±0.02	6.32 ±0.03	4.10 ±0.01	28.6 ±0.4	12.7 ±0.2

Sample name	# of data	MgO/Si[10^{-1}]	MgO_2/Si[10^{-2}]	Fe/Si[10^{-2}]	FeO/Si[10^{-2}]	FeO_2/Si[10^{-2}]	$^{58}Ni/Si[10^{-3}]$	$^{60}Ni/Si[10^{-4}]$
Synthetic forsterite	1	9.25	4.82	0.00	0.00	0.00	0.00	0.00
Iwanai dunite	4	8.08 ±0.32	4.61 ±0.19	1.11 ±0.02	4.42 ±0.13	0.55 ±0.03	6.54 ±0.21	5.47 ±0.13
San Carlos olivine	4	7.98 ±0.11	4.67 ±0.05	1.66 ±0.02	6.60 ±0.14	0.83 ±0.03	6.32 ±0.20	5.13 ±0.19
Miyake olivine	3	7.34 ±0.13	4.39 ±0.15	2.54 ±0.04	9.96 ±0.14	1.30 ±0.06	1.59 ±0.02	1.34 ±0.01
Ol#14	5	7.11 ±0.07	4.30 ±0.12	3.05 ±0.11	12.22 ±0.55	1.67 ±0.11	2.58 ±0.05	2.08 ±0.02
Ol#15	3	6.98 ±0.13	4.41 ±0.06	3.73 ±0.07	15.29 ±0.24	2.20 ±0.04	1.96 ±0.07	1.58 ±0.07

*Analyses were performed using a Cs^+ pimary beam of 10 kV energy and an electron gun for charge compensation. Negative secondary ions of −9.5 kV energy were analyzed at MRP~3000.
**Calculated from Table 1.

Table 4. Comparison of SIMS and EPMA data.

	EPMA	SIMS		
Sample name	$(Fe/Mg)_{atomic}[10^{-2}]$	$(FeO/MgO)_{obs}[10^{-1}]$	$(FeO_2/MgO_2)_{obs}[10^{-1}]$	$(Fe/MgO)_{obs}[10^{-2}]$
Synthetic forsterite	0.01 ± 0.00	0.00	0.00	0.03*
Iwanai dunite	6.30 ± 0.27	0.55 ± 0.02	1.18 ± 0.07	1.38 ± 0.06
San Carlos olivine	9.84 ± 0.07	0.83 ± 0.02	1.77 ± 0.06	2.08 ± 0.06
Miyake olivine	16.84 ± 0.21	1.36 ± 0.02	2.97 ± 0.05	3.43 ± 0.06
Ol#14	22.05 ± 0.68	1.72 ± 0.08	3.88 ± 0.15	4.29 ± 0.21
Ol#15	27.61 ± 0.55	2.19 ± 0.07	4.98 ± 0.14	5.35 ± 0.17

	EPMA	SIMS		
Sample name	$(Ni/Si)_{atomic}[10^{-3}]$	$(^{58}Ni/Si)_{obs}[10^{-3}]$	$(^{60}NiO/Si)_{obs}[10^{-4}]$	$(^{60}NiO/SiO)_{obs}[10^{-2}]$
Synthetic forsterite	0.02 ± 0.02	0.00	0.10*	0.00
Iwanai dunite	8.19 ± 0.19	6.54 ± 0.21	5.47 ± 0.13	3.90 ± 0.12
San Carlos olivine	7.44 ± 0.07	6.32 ± 0.20	5.13 ± 0.19	3.65 ± 0.09
Miyake olivine	1.76 ± 0.02	1.59 ± 0.02	1.34 ± 0.01	1.00 ± 0.01
Ol#14	2.89 ± 0.04	2.85 ± 0.05	2.08 ± 0.02	1.60 ± 0.03
Ol#15	2.08 ± 0.09	1.96 ± 0.07	1.58 ± 0.07	1.20 ± 0.04

*Essentially zero within statistical errors.

Table 5. EPMA/SIMS sensitivity factors.

Sample name	$(Fe/Mg)_{atomic}[10^{-2}]$	$(Fe/Mg)_{atomic}=K_i\times(R_i)_{SIMS}$		
		$R_1=(FeO/MgO)_{SIMS}$	$R_2=(FeO_2/MgO_2)_{SIMS}$	$R_3=(Fe/MgO)_{SIMS}$
		K_1	K_2	K_3
Iwanai dunite	6.30 ± 0.27	1.152 ± 0.069	0.532 ± 0.040	4.578 ± 0.287
San Carlos olivine	9.84 ± 0.07	1.190 ± 0.030	0.555 ± 0.018	4.740 ± 0.141
Miyake olivine	16.84 ± 0.21	1.240 ± 0.022	0.567 ± 0.012	4.917 ± 0.109
Ol#14	22.05 ± 0.68	1.282 ± 0.072	0.568 ± 0.028	5.137 ± 0.301
Ol#15	27.61 ± 0.55	1.260 ± 0.048	0.555 ± 0.019	5.162 ± 0.197
Average		1.225 ± 0.053	0.555 ± 0.014	4.907 ± 0.252

Sample name	$(Ni/Si)_{atomic}[10^{-3}]$	$(Ni/Si)_{atomic}=K_i\times(R_i)_{SIMS}$		
		$R_4=(^{58}Ni/Si)_{SIMS}$	$R_5=(^{60}NiO/Si)_{SIMS}$	$R_6=(^{60}NiO/SiO)_{SIMS}$
		K_4	K_5	K_6
Iwanai dunite	8.19 ± 0.19	1.252 ± 0.050	14.97 ± 0.50	0.2100 ± 0.0081
San Carlos olivine	7.44 ± 0.07	1.177 ± 0.039	14.50 ± 0.55	0.2038 ± 0.0054
Miyake olivine	1.76 ± 0.02	1.104 ± 0.019	13.10 ± 0.18	0.1761 ± 0.0024
Ol#14	2.89 ± 0.04	1.012 ± 0.023	13.87 ± 0.25	0.1808 ± 0.0041
Ol#15	2.08 ± 0.09	1.060 ± 0.058	13.15 ± 0.80	0.1732 ± 0.0095
Average		1.121 ± 0.095	13.92 ± 0.82	0.1888 ± 0.0169

$$(Fe/Mg)_{atomic} \approx (1.23\pm0.05)\times(FeO/MgO)_{SIMS} \approx (0.555\pm0.014)\times(FeO_2/MgO_2)_{SIMS} \approx (4.91\pm0.25)\times(Fe/MgO)_{SIMS}. \quad (4)$$

$$(Ni/Si)_{atomic} \approx (1.12\pm0.10)\times(^{58}Ni/Si)_{SIMS} \approx (13.9\pm0.8)\times(^{60}NiO/Si)_{SIMS} \approx (0.189\pm0.017)\times(^{60}NiO/SiO)_{SIMS}. \quad (5)$$

However, some matrix effect apparently exists. For example, K_1 and K_3 increase with increasing (Fe/Mg) atomic ratio, but K_2 is relatively constant; K_4, K_5 and K_6 decrease with increasing (Fe/Mg) atomic ratio (Table 5). A similar matrix effect is also visible in Table 3, where $(MgO_2/MgO)_{SIMS}$ ratio increases and $(FeO_2/Fe)_{SIMS}$ ratio decreases, respectively, with increasing Fo number of olivine standards. For this matrix effect, the correlation between $(^{60}NiO/SiO)_{SIMS}$ and $(Ni/Si)_{atomic}$ slightly deviates from the linear trend (dashed line, Fig. 4b). In order to improve precision of Ni correlation (Fig. 4b), more data are required for the $(Ni/Si)_{atomic}$ ratio of 0.3–0.7% and >0.9%. At present, however, the above equations may be used for Ni analysis as a rough approximation.

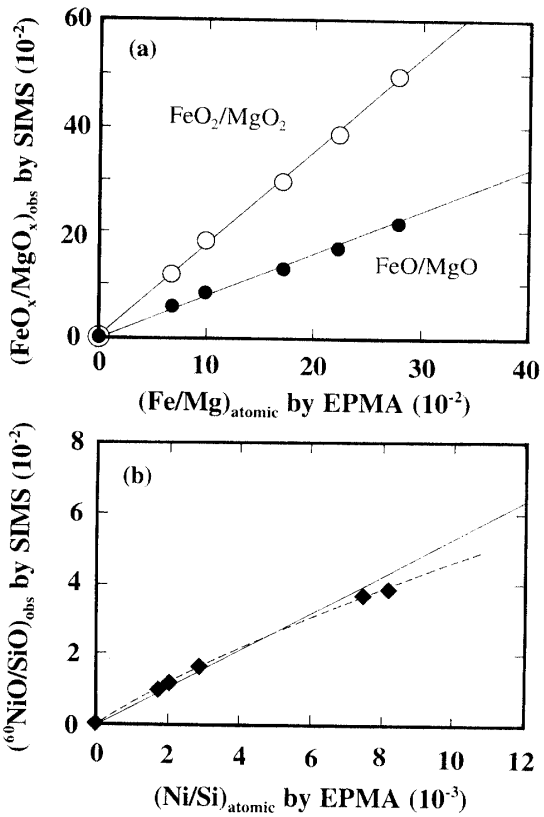

Fig. 4. Calibration of the SIMS data with EPMA data using terrestrial olivine standards of various compositions (Table 1). (a): (FeO/MgO) and (FeO_2/MgO_2) ratios measured by SIMS vs (Fe/Mg) atomic ratios. (b): ($^{60}NiO/SiO$) intensity ratios measured by SIMS vs (Ni/Si) atomic ratios.

3. Results and Discussion

Figure 5 shows a photograph of the Allende chondrule analyzed in the present study. The picture was taken with plane polarized light after the SIMS analysis. The surface of the sample was still covered with thin gold coating and the white spots correspond to the analyzed areas (labeled from A to S), where the gold coating was sputtered away by the Cs^+ beam.

The analytical data for the Fe/(Fe+Mg) ratios and the oxygen isotopic compositions are summarized in Table 6. The Fe/(Fe+Mg) ratios were calculated from the (FeO/MgO) intensity ratios measured with SIMS. Most of the analyzed spots show Mg-rich compositions with the Fe/(Fe+Mg) ratios of 1.6–3.2% for 14 out of 17 points, and only 4 spots (P, K, L and M) show higher ratios (4.4–8.2%).

The oxygen isotope data are expressed as δ-values, *i.e.*, permil deviations from the standard (SMOW) ratios (CRAIG, 1961). San Carlos olivine was used for the oxygen isotope standard, and measured repeatedly before and after the Allende chondrule analysis without changing the instrumental conditions. The results of San Carlos olivine are reproducible (Table 2). The results of the oxygen isotope analyses for Allende

Fig. 5. An Allende chondrule analyzed in the present study. The size of the chondrule is about 1 mm×1.2 mm. The picture was taken with plane polarized light after the SIMS analyses. The surface of the sample was still gold coated and the white spots correspond to the analyzed areas where the gold coating was sputtered away by the Cs^+ beam.

olivines and San Carlos olivine are plotted in the three isotope diagram (Fig. 6). The large open square indicates the average of the San Carlos olivine analyses and all the data are normalized to this point ($\delta^{17}O=2.44‰$ and $\delta^{18}O=4.70‰$). The small open squares show individual results for the San Carlos olivine standard. The relatively small variation for the San Carlos olivine data show good reproducibility of the present analyses. (However, as can be seen in Table 6, duplicate analyses for some points sometimes show larger variations in the observed oxygen isotopic compositions. Since the surface of the Allende chondrule thin section was not as flat as that of San Carlos olivine, I suspect that roughness of the sample surface might affect the reproducibility of the analysis.)

On the other hand, oxygen isotopic compositions in the Allende chondrule show large variations. There seem to be two groups: the first group, consisting of the major-

Table 6. Oxygen isotopic compositions in olivine grains in an Allende chondrule.

Position	Atomic ratios[%]	Oxygen isotopic ratios[‰]	
	Fe/(Fe+Mg)	$\delta(^{17}O)_{SMOW}$	$\delta(^{18}O)_{SMOW}$
A1	2.14 ± 0.09	−9.8 ± 2.9	−3.1 ± 1.5
2		−7.9 ± 2.7	−10.6 ± 1.7
average		−8.8 ± 3.8*	−6.8 ± 5.4*
B	2.11 ± 0.09	−9.8 ± 2.7	−5.5 ± 1.6
C	1.98 ± 0.09	−10.2 ± 2.5	−7.6 ± 1.7
D	1.91 ± 0.08	−6.3 ± 2.5	−9.1 ± 1.7
E	1.64 ± 0.07	−9.8 ± 2.7	−7.5 ± 1.6
F	2.16 ± 0.09	−4.1 ± 2.4	−8.4 ± 1.7
G	2.80 ± 0.12	−11.4 ± 2.5	−9.0 ± 1.6
H	2.88 ± 0.13	−7.2 ± 2.7	−7.5 ± 1.7
J	2.92 ± 0.13	−14.1 ± 2.7	−7.7 ± 1.4
K1	6.72 ± 0.29	−0.5 ± 2.7	0.4 ± 1.7
2		−3.0 ± 2.9	−0.5 ± 1.5
average		−1.8 ± 4.0*	−0.1 ± 2.0*
L1	4.53 ± 0.20	−4.7 ± 2.7	0.4 ± 1.6
2		−6.2 ± 2.8	0.2 ± 1.6
average		−5.4 ± 3.5*	0.3 ± 1.7*
M1	4.43 ± 0.19	−15.2 ± 2.5	−11.7 ± 1.7
2		−8.6 ± 2.8	−3.6 ± 1.6
average		−11.9 ± 5.9*	−7.6 ± 5.7*
N	3.11 ± 0.14	−10.0 ± 2.4	−5.3 ± 1.5
P	8.18 ± 0.35	−1.5 ± 2.5	0.2 ± 1.7
Q	1.77 ± 0.08	−7.5 ± 2.7	−2.1 ± 1.6
R	2.18 ± 0.09	−8.9 ± 2.7	−7.2 ± 1.5
S	3.20 ± 0.14	−11.0 ± 2.6	−8.9 ± 1.6

*Including both reproducibility and counting errors.

ity of the data, shows a relatively ^{16}O-rich composition ($\delta^{17}O = -14$ to -4‰ and $\delta^{18}O = -10$ to -5‰) and the second group, consisting of only 3 points, P, K, and L, shows a relatively ^{16}O-poor composition ($\delta^{17}O = -6$ to -1‰ and $\delta^{18}O$ ~0‰). An interesting observation is that all the points of the second group are relatively Fe-rich with the Fe/(Fe+Mg) ratios of 4.5–8.2% (Table 6) compared with those for the others (1.6–4.4% and mostly <3.2%). They are also located near the boundary (especially, upper boundary in Fig. 5) of the chondrule.

This chondrule seems to be a compound chondrule consisting of two parts: one part occupies most of the left hand side of this chondrule in Fig. 5 with an ellipsoidal shape (I), and the other part occupies the outer part of the right hand side (II). The points J, K and L belong to (II) and the other points belong to (I). However, the distinction between (I) and (II) does not seem to be correlated with the difference in oxygen isotopic compositions. In (I), for example, K and L show the ^{16}O-poor signature but J shows an ^{16}O-rich signature; in (II), only P shows an ^{16}O-poor signature but all the other points show the ^{16}O-rich signature.

Considering relatively large uncertainties in the present analysis (especially so for Allende chondrule data possibly due to surface roughness), the present results must be considered still rather preliminary. However, the overall trend of the present results

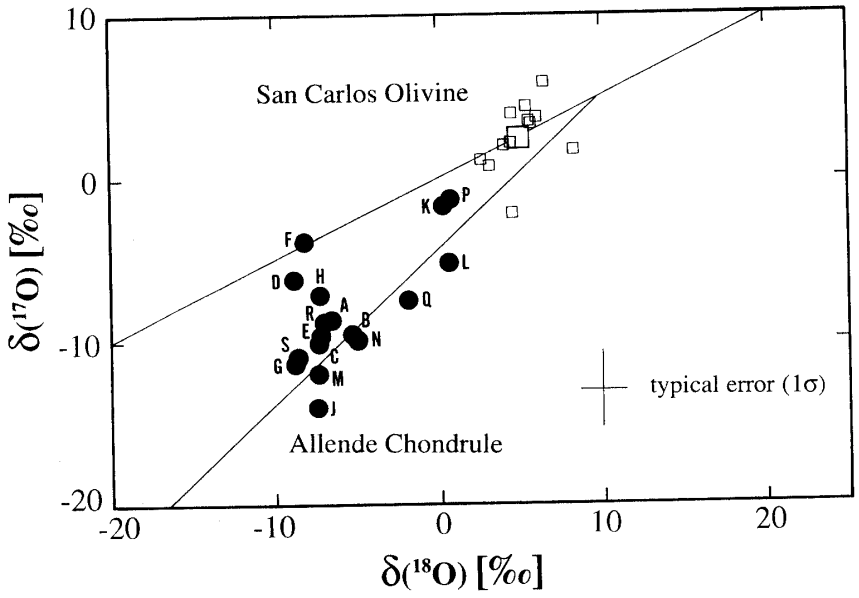

Fig. 6. The results of oxygen isotope analyses for olivine grains in an Allende chondrule (closed circles) and those for San Carlos olivine used as a standard (small open squares). The large open square shows the average of the San Carlos olivine data and all the data are normalized to this point ($\delta^{17}O = 2.44‰$ and $\delta^{18}O = 4.70‰$). The line with a slope of ~1/2 is the terrestrial fractionation line and that with a slope of ~1 is the CAI fractionation line (CLAYTON et al., 1976).

may be real. First of all, the average of the main cluster is located near or slightly above the Allende mixing line (somewhere around $\delta^{17}O \sim -10‰$ and $\delta^{18}O \sim -8‰$). This is not an artifact because an instrumental mass fractionation can move the data only in the direction of a slope-1/2 line in this figure. Also, existence of the two groups, ^{16}O-rich and ^{16}O-poor, may be real. The correlation between oxygen isotopic compositions and Fe contents may support this. The present results suggest that there is heterogeneity in oxygen isotopic composition even within a single chondrule.

It would be important to note that P and F belong to the same single olivine grain, although they seem to have different oxygen isotope signatures. If this is the case, such an oxygen isotope signature must be introduced *after* formation of the olivine grain. (One problem for the point P is that the upper margin of the beam was located outside this olivine grain as can be seen in Fig.5, and therefore, there may be some contribution from the material of this area. However, the analyzed area was limited to the 12 $\mu m\phi$ area of the center of the beam, and oxygen is the major element of olivine, I expect such a contribution to be small.) However, considering the precision of the present data, an instrumental mass fractionation cannot be ruled out for the cause of this observation. More data (and better precision) are required to discuss such details of the oxygen isotopic composition in Allende chondrules.

It is interesting to compare the present results with those obtained by CLAYTON *et al.* (1983) and RUBIN *et al.* (1990). A difference lies in the range of the obtained oxygen isotopic compositions. The present study gives $\delta^{18}O$ values down to $\sim -10‰$

(and the average of the main cluster seems to have $\delta^{18}O \sim -8‰$), which is much lower than the value ($\delta^{18}0 \sim -3‰$) obtained using gas mass spectrometry for Allende chondrules (CLAYTON *et al.*, 1983). The reason for this is not certain at present. It may be simply a problem of statistics. An encouraging observation, however, is that the average composition of the main cluster is located nearly on the extension of the Allende chondrule correlation line (CLAYTON *et al.*, 1983, 1993).

A similarity exists between the present results and those by RUBIN *et al.* (1990). The main cluster (having a ^{16}O-rich composition) shows a lower Fe content and the other group (having a ^{16}O-poor composition) shows a higher Fe content. This is consistent with a positive correlation between the Fe-content and $\delta^{18}O$ value observed by RUBIN *et al.* (1990), though the ranges of the observed Fe contents are also different (1.6–8.2 wt% in the present study and 3–26 wt% in RUBIN *et al.*, 1990). A similar correlation was also reported by WEINBRUCH *et al.* (1993) for FeO-poor isolated olivine and FeO-rich olivine rims and matrix olivines. Using SIMS, they observed a ^{16}O-rich composition for the former and a ^{16}O-poor composition for the latter (with some exceptions of ^{16}O-rich matrix olivine grains). However, the FeO contents of their FeO-rich rims and matrix olivines are also very high (20–41 wt% FeO, or $Fe/(Fe+Mg)_{atomic} = 12.3–18.7\%$), which is different from the present case. Considering the similarity in the correlations between FeO contents and $\delta^{18}O$ values observed in the present study and by others, a similar process (*e.g.*, reactions with the nebular gas having a ^{16}O-poor and Fe-rich composition) may be responsible for the correlations (*e.g.*, RUBIN *et al.*, 1990; WEINBRUCH *et al.*, 1993), though it is not conclusive.

However, if data for olivine grains in ordinary chondrites are taken into account, the situation seems to be more complicated. SAXTON *et al.* (1996) conducted a SIMS analysis for isolated olivine grains with FeO-poor ($Fe/(Fe+Mg)_{atomic} < 5\%$) cores and FeO-rich ($Fe/(Fe+Mg)_{atomic} = 15–20\%$) rims in Julesburg ordinary chondrite (L3.7). They found that the rimmed isolated olivine grains have variable oxygen isotopic compositions with $\delta^{18}O$ values down to $\sim -10‰$ but that the core-rim difference within a single grain is usually small compared to the total variation in different grains. They also analyzed an olivine-rich chondrule but found that it has an oxygen isotopic composition very close to that of bulk Julesburg.

As shown above, it is now observed by several authors that some isolated olivine grains in CV (Allende) and ordinary (Julesburg) chondrites have ^{16}O-rich compositions (*e.g.*, $\delta^{18}O \sim -10‰$). However, the present results, though still rather preliminary, suggest that olivine grains in a chondrule also have a similar ^{16}O-enrichment. The present study also suggests that there is heterogeneity in oxygen isotopic composition even within a single chondrule and that there is a correlation between the $\delta^{18}O$ value and FeO-content, which is more or less similar to those found by some authors (RUBIN *et al.*, 1990; WEINBRUCH *et al.*, 1993). However, the present study is limited only to a single chondrule in Allende meteorite. Furthermore, it is necessary to improve precision of the SIMS data to understand fine structure of the oxygen isotopic composition in chondrules or olivine grains. Apparently further studies are required to fully understand oxygen isotope signatures in chondrules, isolated olivines (their cores and rims) and matrix olivines, their genetic relations, and to understand the processes worked in the early solar system. The SIMS technique for the *in situ*

analysis of oxygen isotopes in meteorites developed in the present study and in the work by other authors would play an important role in this field.

Acknowledgments

I express thanks to Dr. Linda SCHRAMM, National Museum of Natural History, for providing San Carlos olivine and Burma spinel. Ms. Ifatt JABEEN and Dr. Minoru KUSAKABE at Institute for Study of Earth's Interior, Okayama University, kindly measured the oxygen isotopic compositions of Burma spinel and San Carlos olivine with gas mass spectrometry using a laser-fluorination method. Dr. Kazuhito OZAWA, Geological Institute, University of Tokyo, kindly provide terrestrial olivine standards and conducted EPMA analyses on them. I also thank Prof. Ernst ZINNER, Washington University, and Dr. Gary HUSS, Caltech, for useful suggestions for the SIMS analysis and thank Dr. Naoji SUGIURA for his encouragement, valuable discussions, and help in installation and operation of the instrument. I also thank Dr. Hisayoshi YURIMOTO and two anonymous reviewers, who gave valuable comments and suggestions, which improved the manuscript both in its contents and in English. An anonymous reviewer kindly informed me of a reference about the oxygen isotopic composition of San Carlos olivine.

References

ANDERS, E., VIRAG, A., ZINNER, E. and LEWIS R. S. (1991): ^{16}O and ^{26}Al in the early solar system: Clues from meteoritic Al_2O_3. Astrophys. J., **373**, L77–L80.

BAERTSCHI, P. (1976): Absolute ^{18}O content of standard mean ocean water. Earth Planet. Sci. Lett., **31**, 341–344.

CLAYTON, R. N. (1993): Oxygen isotopes in meteorites. Ann. Rev. Earth Planet. Sci., **21**, 115–149.

CLAYTON, R. N., GROSSMAN, L. and MAYEDA, T. K. (1973): A component of primitive nuclear composition in carbonaceous meteorites. Science, **182**, 485–488.

CLAYTON, R. N., ONUMA, N. and MAYEDA, T. K. (1976): A classification of meteorites based on oxygen isotopes. Earth Planet. Sci. Lett., **30**, 10–18.

CLAYTON, R. N., ONUMA, N., IKEDA, Y., MAYEDA, T. K., HUTCHEON, I. D., OLSEN, E. J. and MOLINI-VESKO, C. (1983): Oxygen isotopic compositions of chondrules in Allende and ordinary chondrites. Chondrules and Their Origins, ed. by E. A. KING. Houston, Lunar Planet. Inst., 37–43.

CLAYTON, R. N., MAYEDA, T. K., GOSWAMI, J. N. and OLSEN, E. J. (1993): Oxygen isotope studies of ordinary chondrites. Geochim. Cosmochim. Acta, **55**, 2317–2337.

CHOI, B.-G., MCKEEGAN, K. D., LESHIN, L. A. and WASSON, J. T. (1997): Origin of magnetite in oxidized CV chondrites: *in situ* measurement of oxygen isotope compositions of Allende magnetite and olivine. Earth Planet. Sci. Lett., **146**, 337–349.

CRAIG, H. (1961): Standard for reporting concentrations of deuterium and oxygen-18 in natural waters. Science, **133**, 1833–1834.

EILER, J. M., FARLEY, K. A., VALLEY, J. W., STOLPER, E. M., HAURL, E. H. and CRAIG, H. (1995): Oxygen isotope evidence against bulk recycled sediment in the mantle sources of Pitcairn Island lavas. Nature, **377**, 138–141.

FAHEY, A. J., GOSWAMI, J. N., MCKEEGAN, K. D. and ZINNER, E. K. (1987): ^{16}O excesses in Murchison and Murray hibonites: A case against a late supernova injection origin of isotopic anomalies in O, Mg, Ca, and Ti. Astrophys. J., **323**, L91–L95.

GNAZER, H. and HUTCHEON, I. D. (1988a): Significance of isotope effects for secondary-ion emission models. Phys. Rev., **38**, 11112–11117.

GNAZER, H. and HUTCHEON, I. D. (1988b): Preferential emission of lighter isotopes in the initial stage of sputtering. Surface Sci., **195**, 499–512.

HERVIG, R. L. and STEELE, I. M. (1992): Oxygen isotopic analysis of Allende olivine by ion microprobe and implications for chondrule origin. Lunar and Planetary Science XXIII. Houston, Lunar Planet. Inst., 525–526.

HERVIG, R .L. and STEELE, I. M. (1995): Oxygen isotopic microanalysis of isolated forsterites form Ornans (C3O) and Murchison (C2). Lunar and Planetary Science XXVI. Houston, Lunar Planet. Inst., 589–590.

HIYAGON, H. (1996): Oxygen isotope analysis of rock samples using CAMECA ims-6f: preliminary experiments. Todai Int. Symp. on Cosmochronology and Isotope Geoscience (abstr.), 98–101.

HOPPE, P., KURAT, G., WALTER, J. and MAURETTE, M. (1995a): Trace elements and oxygen isotopes in a CAI-bearing micrometeorite from Antarctica. Lunar and Planetary Science XXVI. Houston, Lunar Planet. Inst., 623–624.

HOPPE, P., AMARI, S., ZINNER, H. and LEWIS, R. S. (1995b): Isotopic compositions of C, N, O, Mg and Si, trace element abundances, and morphologies of single circumstellar graphite grains in four density fractions from the Murchison meteorite. Geochim. Cosmochim. Acta, **59**, 4029–4056.

HUSS, G. R., FAHEY, A. J., GALLINO, R. and WASSERBURG, G. J. (1994): Oxygen isotopes in circumstellar Al_2O_3 grains from meteorites and stellar nucleosynthesis. Astrophys. J., **430**, L81–L84.

HUTCHEON, I. D., HUSS, G. R., FAHEY, A. J. and WASSERBURG, G. J. (1994): Extreme ^{26}Mg and ^{17}O enrichments in an Orgueil corundum: Identification of a presolar oxide grain. Astrophys. J., **425**, L97–L100.

JULL, A. J. T. (1982): Variations of isotopic discrimination in secondary ion mass spectrometry. Int. J. Mass Spec. Ion Phys., **41**, 135–141.

KURAT, G., HOPPE, P., WALTER, J., ENGRAND, C. and MAURETTE, M. (1994): Oxygen isotopes in spinels from Antarctic micrometeorites. Meteoritics, **29**, 487–488.

LESHIN, L. A., RUBIN, A. E. and MCKEEGAN, K. D. (1997): The oxygen isotopic composition of olivine and pyroxene from CI chondrites. Geochim. Cosmochim. Acta, **61**, 835–845.

MATTEY, D. and MACPHERSON, C. (1993): High-precision oxygen isotope microanalysis of ferromagnesian minerals by laser-fluorination. Chem. Geol. (Isot. Geosci. Sect.), **105**, 305–318.

MCKEEGAN, K. D. (1987a): Oxygen isotopes in refractory stratospheric dust particles: Proof of extraterrestrial origin. Science, **237**, 1468–1471.

MCKEEGAN, K. D. (1987b): Ion microprobe measurements of H, C, O, Mg, and Si isotopic abundances in individual interplanetary dust particles. Ph.D. Thesis, Washington University.

MCKEEGAN, K. D., WALKER, R. M. and ZINNER, E. (1985): Ion microprobe isotopic measurements of individual interplanetary dust particles. Geochim. Cosmochim. Acta, **49**, 1971–1987.

MCKEEGAN, K. D., LESHIN, L. A., RUSSEL, S. S. and MACPHERSON, G.J. (1996): *In situ* measurement of O isotopic anomalies in a type B Allende CAI. Meteoritics, **31**, A87.

NIEDERER, F. R., PAPANASTASSIOU, D. A. and WASSERBURG, G. J. (1981): The isotopic composition of titanium in the Allende and Leoville meteorites. Geochim. Cosmochim. Acta, **45**, 1017–1031.

RUBIN, A. E., WASSON, J. T., CLAYTON, R. N. and MAYEDA, T. K. (1990): Oxygen isotopes in chondrules and coarse-grained chondrule rims from the Allende meteorite. Earth Planet. Sci. Lett., **96**, 247–255.

SAXTON, J. M., LYON, I.C. and TURNER, G. (1995): Oxygen isotopes in forsterite grains from Julesburg and Allende: Oxygen-16-rich material in an ordinary chondrite. Meteoritics, **30**, 571–572.

SAXTON, J. M., LYON, I. C. and TURNER, G. (1996): Oxygen-16-rich olivine in the Julesburg ordinary chondrite. Meteoritics, **31**, A123.

SHIMIZU, N. and HART, S. R. (1982): Applications of the ion microprobe to geochemistry and cosmochemistry. Ann. Rev. Earth Planet. Sci., **10**, 483–526.

SLODZIAN, G. (1980): Microanalyzers using secondary ion emission. Adv. Electrnics Electron Phys., Suppl., **13B**, 1–44.

VIRAG, A., ZINNER, E., AMARI, S. and ANDERS, E. (1991): An ion probe study of corundum in the Murchison meteorite: Implications for ^{26}Al and ^{16}O in the early solar system. Geochim. Cosmochim. Acta, **55**, 2045–2062.

WEINBRUCH, S., ZINNER, E. K., El GORESY, A., STEELE, I. M. and PALME, H. (1993): Oxygen isotopic com-

position of individual olivine grains from the Allende meteorite. Geochim. Cosmochim. Acta, **57**, 2649–2661.

YURIMOTO, H., NAGASAWA, H., MORI, Y. and MATSUBAYA, O. (1994): Micro-distribution of oxygen isotopes in a refractory inclusion from the Allende meteorite. Earth Planet. Sci. Lett., **128**, 47–53.

ZINNER, E., FAHEY, A. J. and MCKEEGAN, K. D. (1986): Characterization of electron multipliers by charge distributions. Secondary Ion Mass Spectrometry (SIMS V), ed. by A. BENNINGHOVEN *et al.* Berlin, Springer, 170–172.

(Received August 28, 1996; Revised manuscript accepted May 2, 1997)

Appendix

A. Field aperture position vs instrumental mass fractionation

Oxygen isotope measurements were performed for San Carlos olivine with various positions of the field aperture relative to the primary beam image. The analytical condition was similar to that described in text, but the primary beam size was smaller (~40 μm in diameter). The size of the field aperture corresponded to ~12 μm area on the beam image. The primary beam intensity was ~0.3 nA. The results are demonstrated in Fig. A1. The observed $^{18}O/^{16}O$ ratios are dependent on the field aperture position and the overall variation is ~10‰, much higher than the statistical errors (~2‰). The smaller beam size used in this experiment might enhance the dependence of the instrumental mass fractionation on the field aperture position, however.

B. Entrance slit position vs instrumental mass fractionation

Oxygen isotope measurements were performed for San Carlos olivine with various entrance slit positions. The analytical condition was the same as that in Appendix A, but the field aperture was centered on the beam image. The entrance slit width was

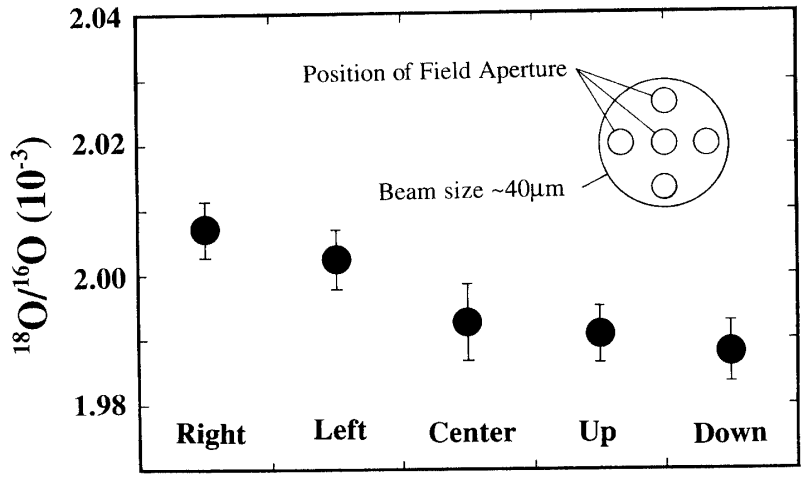

Fig. A1. Instrumental mass fractionation in oxygen isotopes for various positions of the field aperture relative to the beam position.

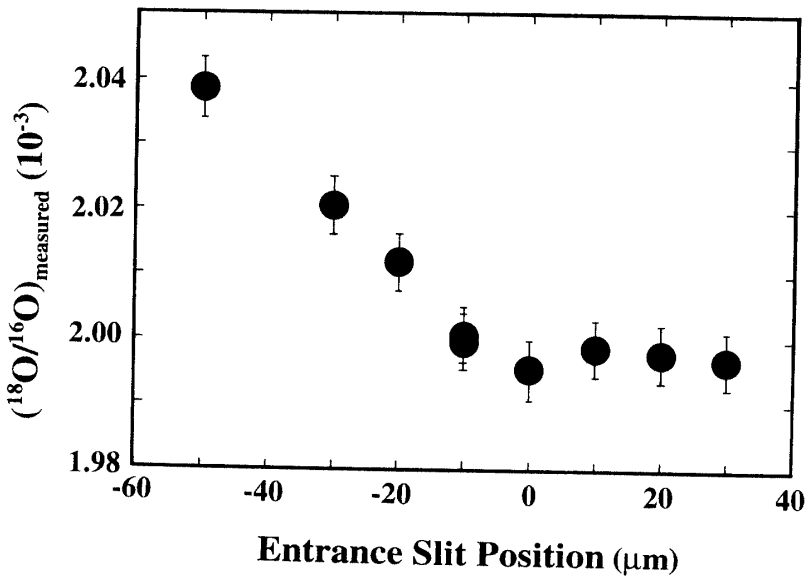

Fig. A2. Instrumental mass fractionation in oxygen isotopes for various positions of the entrance slit.

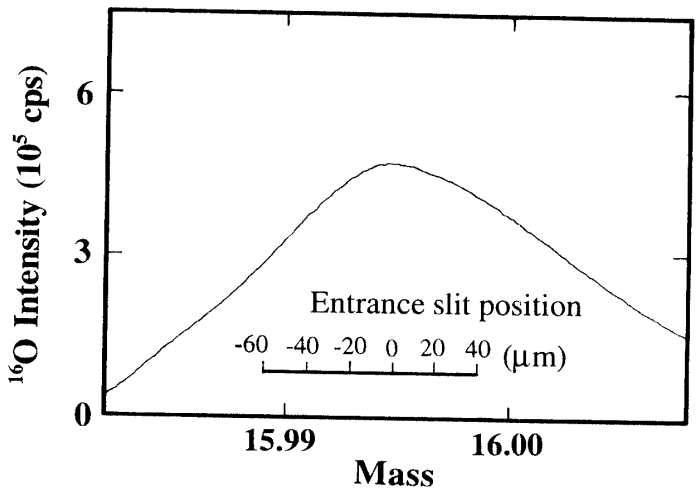

Fig. A3. The shape of the crossover image obtained by scanning the ^{16}O peak with a full width for the entrance slit and a narrow width for the exit slit. The approximate entrance slit position relative to the crossover image corresponding to Fig. 8 is also shown.

~5 μm. The results are shown in Fig. A2. The entrance slit position of 0 μm corresponds approximately to the center of the crossover image. The measured $^{18}O/^{16}O$ ratios increased greatly when the entrance silt position was shifted to the left (from -10 μm to -50 μm), but showed no significant change for the positions from 0 μm to 30 μm. The cause for such an asymmetrical results is not certain, but possibly it may be related to the asymmetry in the crossover image. The shape of the crossover image is demonstrated in Fig. A3. This diagram was obtained by setting the exit slit width narrow (*i.e.*, the same width as that of the entrance slit image at the exit slit position),

then opening the entrance slit wide to admit all the beam at the crossover position, and simply scanning the magnetic field instead of moving the entrance slit. The approximate position of the entrance slit corresponding to Fig. A2 is also shown in the figure. The shape of the crossover image is not completely symmetrical but the left side of the profile has a steeper slope. The results suggest that tuning of the secondary ion optics to get a symmetrical crossover image and positioning of the entrance slit on the center of the crossover image is crucial for reproducible analyses of oxygen isotopes (and also for high resolution isotope analysis in general).

C. Instrumental mass fractionation during the initial stage of sputtering

Oxygen isotope measurements were performed for San Carlos olivine to examine the instrumental mass fractionation at the initial stage of sputtering. A thin gold coating (~200 Å) was applied to the polished surface of the sample. The measurements were performed with a 10 kV Cs^+ primary beam, -9.5 kV secondary ion acceleration voltage, and using the normal-incidence electron gun (NEG). The primary beam was circular and homogeneous with a diameter of ~30 μm and with an intensity of 0.08 nA, corresponding to a beam density of $\sim 3 \times 10^{-6}$ A/cm^2, which was about half of that used in the Allende chondrule analysis ($\sim 6 \times 10^{-6}$ A/cm^2). A larger field aperture corresponding to a ~35 $\mu m\phi$ field image was used to admit all the secondary beam for the analysis. Only two isotopes, ^{16}O and ^{18}O, were analyzed; the ^{16}O intensity was measured with a Faraday cup and the ^{18}O intensity with an electron multiplier-based ion counting system. A dead time correction, though very small, was applied for the ^{18}O intensity. The base line for the Faraday cup was measured at mass 17.8, where no peaks were expected, and used for correcting the ^{16}O intensity. The sensitivity ratio between the two detectors was very close to unity, but it was not determined precisely, so that no correction for this was applied in this experiment. Mass resolution was set to be ~2000 to separate ^{18}O and $^1H_2{}^{16}O$ peaks. The entrance slit position was centered on the crossover image. The relatively wide slit width might also help stabilizing the instrumental mass fractionation. The waiting times and counting (integration) times for ^{16}O, mass 17.8 and ^{18}O were 1, 0.2 and 0.5 (s) and 1, 1 and 2 (s), respectively. Each measurement consists of 5 or 10 blocks with 10 cycles (*i.e.*, a total of 50 or 100 cycles) and took about 10 or 20 min. The ^{16}O intensity increased very rapidly during the first 10 min, so that the intensity change within one cycle could not be neglected. Hence, the intensity change of the normalization peak (^{16}O) was taken into account in the calculation of the $^{18}O/^{16}O$ ratio. The analyses were performed for three different points of San Carlos olivine. Each point was analyzed repeatedly until the measured $^{18}O/^{16}O$ ratio as well as the ^{16}O intensity became stable. The results are shown in Table A1 and Fig. A4. Open squares show the ^{16}O intensity and closed circles show the measured $^{18}O/^{16}O$ ratios (each large circle stands for the average of 5 blocks (consisting of 50 cycles) and each small circle for a single block (consisting of 10 cycles)). The results were very reproducible for the three points analyzed. The measured $^{18}O/^{16}O$ ratio always started from a surprisingly low value and increased for 10–15 min until an steady-state value was attained. Note that this was not caused by the contribution of surface-contaminating oxygen. In fact, the intensity of surface-contaminating ^{16}O, observed at the very beginning of the analysis, decreased during sputtering the gold

Table A1. Oxygen isotope analysis in the initial stage of sputtering.

Position	Analysis#-Block#	Time* (min)	^{16}O Intensity (10^6cps)	$^{18}O/^{16}O$*** (10^{-3})
Pos.#1	SC14 –1	6.5	7.70 ± 0.70	1.9465 ± 0.0033
	–2	7.5	8.70 ± 0.50	1.9569 ± 0.0033
	–3	8.5	9.40 ± 0.30	1.9614 ± 0.0055
	–4	9.5	9.90 ± 0.20	1.9585 ± 0.0032
	–5	10.5	10.25 ± 0.20	1.9670 ± 0.0034
	SC15 –1	13.5	11.00 ± 0.12	1.9768 ± 0.0033
	–2	14.5	11.23 ± 0.11	1.9759 ± 0.0032
	–3	15.5	11.35 ± 0.07	1.9791 ± 0.0036
	–4	16.5	11.45 ± 0.08	1.9848 ± 0.0027
	–5	17.5	11.55 ± 0.05	1.9811 ± 0.0022
	–6	18.5	11.64 ± 0.06	1.9851 ± 0.0032
	–7	19.5	11.74 ± 0.05	1.9804 ± 0.0028
	–8	20.5	11.75 ± 0.05	1.9846 ± 0.0186
	–9	21.5	11.75 ± 0.05	1.9879 ± 0.0022
	–10	22.5	11.75 ± 0.05	1.9851 ± 0.0029
	SC16 (5 blocks)	28	11.90 ± 0.12	1.9870 ± 0.0012
	SC17 (5 blocks)	33.5	12.12 ± 0.11	1.9903 ± 0.0014
	SC18 (5 blocks)	38.5	12.25 ± 0.15	1.9886 ± 0.0014
	SC19 (5 blocks)	44	12.38 ± 0.08	1.9924 ± 0.0014
Pos.#2	SC20 –1	8.5	10.60 ± 0.27	1.9613 ± 0.0041
	–2	9.5	11.03 ± 0.15	1.9676 ± 0.0041
	–3	10.5	11.40 ± 0.22	1.9704 ± 0.0032
	–4	11.5	11.43 ± 0.18	1.9742 ± 0.0045
	–5	12.5	11.78 ± 0.11	1.9771 ± 0.0030
	SC21 (5 blocks)	16	12.21 ± 0.09	1.9798 ± 0.0014
	SC22 (5 blocks)	21.5	12.32 ± 0.09	1.9895 ± 0.0014
	SC23 (5 blocks)	26.5	12.40 ± 0.07	1.9909 ± 0.0014
	SC24 (5 blocks)	31.5	12.48 ± 0.10	1.9921 ± 0.0014
	SC25 (5 blocks)	37	12.44 ± 0.09	1.9917 ± 0.0014
Pos.#3	SC26 –1	5.5	5.40 ± 1.00	1.9247 ± 0.0081
	–2	6.5	7.30 ± 0.80	1.9350 ± 0.0045
	–3	7.5	8.70 ± 0.60	1.9485 ± 0.0054
	–4	8.5	9.70 ± 0.35	1.9599 ± 0.0029
	–5	9.5	10.30 ± 0.30	1.9640 ± 0.0028
	–6	10.5	10.80 ± 0.20	1.9670 ± 0.0038
	–7	11.5	11.05 ± 0.15	1.9704 ± 0.0033
	–8	12.5	11.30 ± 0.10	1.9669 ± 0.0028
	–9 **	13.5	11.45 ± 0.08	1.9394 ± 0.0321**
	–10	14.5	11.55 ± 0.08	1.9735 ± 0.0025
	SC27 (5 blocks)	20	11.92 ± 0.14	1.9855 ± 0.0016
	SC28 (5 blocks)	25.5	12.06 ± 0.07	1.9848 ± 0.0017
	SC29 (5 blocks)	31	12.13 ± 0.08	1.9891 ± 0.0016
	SC30 (5 blocks)	36.5	12.15 ± 0.08	1.9908 ± 0.0015
	SC31 (5 blocks)	42	12.10 ± 0.07	1.9901 ± 0.0013

* Integrated sputtering time at the middle of each analysis (approximate value).
** Data not adopted due to a large spike on mass 16 during the analysis.
*** Errors are 1σ.

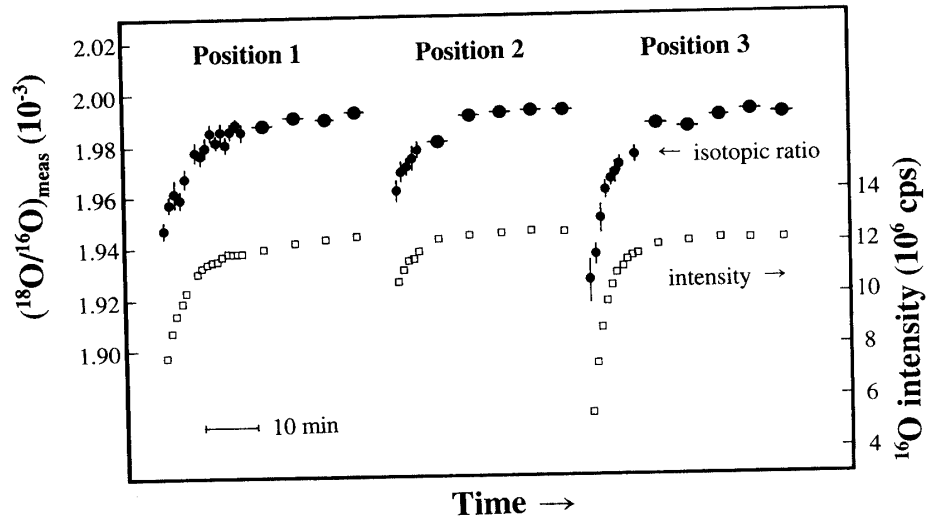

Fig. A4. Instrumental mass fractionation in oxygen isotopes during the initial stage of sputtering. Open squares show the ^{16}O intensity and closed circles show the measured $^{18}O/^{16}O$ ratios (each large circle stands for the average of 5 blocks (50 cycles) and each small circle for a single block (10 cycles)).

layer down to a few thousand cps, which was by a factor of ~10^4 lower than the ^{16}O signal from the sample (~10^7 cps). Therefore, the observed change in the $^{18}O/^{16}O$ ratio was most likely caused by modifications of the near-surface region of the sample by the sputtering process before a steady-state was attained. Similar phenomena are reported by GNAZER and HUTCHEON (1988b) for isotopes of Li, Ti, and some other elements. They observed large enrichment of light isotopes (by 54‰ for $^6Li/^7Li$, 63‰ for $^{46}Ti/^{50}Ti$, etc.) at the initial stage of sputtering, which is also the case for the present results. This is probably the first report of such a phenomenon for oxygen isotopes. Note that the beam density used in the Allende analysis was about 2 times stronger than that used in this experiment and that the Allende analysis was performed only after the $^{16}O^-$ beam intensity became very stable, *i.e.*, typically >15 min after onset of the beam. Hence, this effect may not be important in the analysis of the Allende chondrule.